New Backstepping-DSOGI hybrid control applied to a Smart-Grid Photovoltaic System

Salim Nebili [1†], Ibrahim Benabdallah 2[††] and Cherif Adnene[†]
salim.nebili@tunisietelecom.tn ibrahim.benabdallah@gmail.com adnen2fr@yahoo.fr
Faculty of sciences of Tunisia, Dept. of physics, Analysis and treatment of electrical and energetic systems, ElmanarI, Tunis, Tunisia

Summary
In order to overcome the power fluctuation issues in photovoltaic (PV) smart grid-connected systems and the inverter nonlinearity model problem, an adaptive backstepping command-filter and a double second order generalized Integrators (DSOGI) controller are designed in order to tune the AC current and the DC-link voltage from the DC side. Firstly, we propose to present the filter mathematical model throughout the PV system, at that juncture the backstepping control law is applied in order to control it, Moreover the command filter is bounded to the controller aiming to exclude the backstepping controller differential increase. Additionally, The adaptive law uses Lyapunov stability criterion. Its task is to estimate the uncertain parameters in the smart grid-connected inverter. A DSOGI is added to stabilize the grid currents and eliminate undesirable harmonics meanwhile feeding maximum power generated from PV to the point of common coupling (PCC). Then, guaranteeing a dynamic effective response even under very unbalanced loads and/or intermittent climate changes. Finally, the simulation results will be established using MATLAB/SIMULINK proving that the presented approach can control surely the smart grid-connected system.

Key words:
Load Flow Analysis, Motor Start Up analysis, THD rate, Real plant.

1. Introduction

Presently, traditional controllers encounter new issues typology with the massive number of grid-connected photovoltaic systems (PVs) in their way to maintain a totally effective and reliable [1] grid. Drawn hereunder in Fig.1 is the figure of our designed system. Many parameters are essential to be taken into consideration [2]; such as meteorological impacts like temperature, irradiation and wind speed. Furthermore, there is some important predominant other factors like the inverter comportment, the PV command laws and the load state [3].

There is a special sight seen from inverter design and control point of view to merge the output electrical power quality of the used strategy.

The intercepted power from the PV system part is converted to a useful and optimal power within the restricted standards. Then, any potential upcoming atmospheric changes couldn't perturb the power quality;[4] like power factor which is close to the unity, Unsignifying injected harmonic current rate into the grid besides minimal reactive power.

In this same axis, there are several papers in literature that accord importance for control by using automatic sophisticated methods and technical conception in order to achieve a robust chain, including several estimation errors reduced by the mean of algorithms such as the backstepping control.

The Authors in [5] agree with the finite time stability and control for a class of uncertain variable fractional order nonlinear systems. They develop a variable fractional Lyapunov direct method in order to afford the stability proof of the considered system basis. They applied the sliding mode control method for uncertain variable fractional order systems robust control and then they eliminate the chattering phenomenon based on the proposed stability criterion.

In [6] an improved finite control set model predictive voltage control proposed for the distributed energy resource in AC islanded microgrid was proposed. They proposed a control approach that uses mathematical models of the power converter to anticipate the voltage response for possible switching states in every sampling period in addition to a dual-objective cost function to regulate the output voltage as well as load current under fault condition and non-linear loading conditions.

Whereas, in [7] they addressed a practical finite-time leader-following formation controller design for the second-order stochastic Lipchitz nonlinear systems under uncertain communication environments and external disturbances. They proposed backstepping sliding-mode controller guarantees that all the signals in the closed-loop system remain bounded in probability and the norm of sliding trajectories converge almost surely infinite-time to an arbitrary small neighborhood of origin, which can be called almost-surely practical finite-time formation.

The work in [8], an adaptive control scheme based on command-filtered backstepping was presented using a class

Manuscript received March 17, 2022
Manuscript revised March 27, 2022
https://doi.org/10.22937/IJCSNS.2022.22.4.1

of uncertain multiple-input-multiple-output MIMO strict-feedback nonlinear systems. Within the last proposed scheme, extreme machine learning (EML) with random hidden nodes was used in the controller in order to approximate unknown functions besides a smooth projection algorithm that was adopted to adjust online estimated controller parameters such that the parameter estimates can be ensured. Moreover, some classical command filters have been designed to produce virtual control signals and their derivations thus the analytic calculation of the partial derivative's virtual control signals has been removed. Likewise, the authors exposed some other filters aiming to generate filtered tracking error compensation.

In [9] they presented a nonlinear coupled three tank system control. In which they designed a command-filtered backstepping control method, dedicated for the third tank of the INTECO three-tank model's fluid level tracking. Meanwhile, comparing the pump control signal outputs with the backstepping controller references. They avoid the high frequency noise induced by the command signal derivatives into the control signal by the low pass filter use.

Whereas in [10] a robust adaptive synchronization steering control design with set performance of the supply ship during underway refill using the adaptive technique derived to estimate the unidentified environmental turbulences bounds. The prescribed performance control technique has been introduced in order to guarantee the prescribed transient and steady-state performance of synchronization control and the command-filtered backstepping approach employed to avoid the direct analytic derivation of the virtual stabilizing function in the conventional backstepping.

As a nonlinear control approach, the backstepping, which is widely used in grid-connected system is considered to deal with the nonlinearity and uncertainty [5-13]. Then, a backstepping controller stabilizes the DC side voltage and ensures that the total harmonic distortion rate of the AC side is within the permitted range.

Though, due to some main backstepping control weaknesses, like the virtual control derivative and control saturation problems which can upsurge the calculation time amount and then controller performance.

Some approaches have been put forward to solve this shortcoming. In literature, there's two ways to deal with that; firstly the dynamic surface control and second the command-filter control. In which command-filtered backstepping is more trustworthy than dynamic surface control [14-15]. Amplitude, speed and bandwidth constraints are introduced into the command filtering process, which are more convenient for modulating and restricting virtual control signals and real control signals so as to meet the actualized control requirements.

As a contribution in this paper, an improved adaptive command-filtered backstepping controller tied to a DSOGI is designed for the inverter control. In the last proposed controller, an adaptive law based on Lyapunov stability theory is presented for the uncertain parameters estimation purpose counting the DC link capacitor, the output resistance and the inductance related to the grid-connected inverter.

In the controller design process, the command filter and the compensation are used to solve the problems of the differential expansion about virtual control signal and the control input saturation. Meanwhile, control system stability is presented as asymptotically stable using the Lyapunov's stability theory.

The DSOGI is intended based on voltage equations written in complex representation in various reference frames that match with the harmonic current. Thus, a decoupling control in each reference frame could be attained which has been hard to achieve in the past. That will improve the harmonic current control transient response by decoupling control in several reference frames besides the first overshoot attenuation locked down to regulatory limits.

In Section 2, we propose to establish the mathematical inverter and filter modelling. Whereas, In Section 3, the controller is derived and the stability of the system is proved by Lyapunov's stability theory. The advanced nature of the designed controller is demonstrated in MATLAB/Simulink and presented in Section 4. Finally, conclusions are drawn in Section 5.

2. Mathematical inverter and filter modelling:

Fig.1 illustrates the overall PV system.

$$\begin{Bmatrix} V_{fd} = R_T * I_{Td} + L_{Td}\frac{dI_{Td}}{dt} - W_S * L_{Tq} * I_{Tq} + V_{rd} \\ V_{fq} = R_T * I_{Tq} + L_{Tq}\frac{dI_{Tq}}{dt} + W_S * L_{Td} * I_{Td} + V_{rd} \end{Bmatrix} \quad (1)$$

$$\begin{Bmatrix} \frac{dI_{Td}}{dt} = \frac{V_{fd}}{L_{Td}} - \frac{R_T}{L_{Td}} * I_{Td} + W_S * \frac{L_{Tq}}{L_{Td}} * I_{Tq} - \frac{V_{rd}}{L_{Td}} \\ \frac{dI_{Tq}}{dt} = \frac{V_{fq}}{L_{Tq}} - \frac{R_T}{L_{Tq}} * I_{Tq} - W_S * \frac{L_{Td}}{L_{Tq}} * I_{Td} - \frac{V_{rq}}{L_{Tq}} \end{Bmatrix} \quad (2)$$

$$\begin{Bmatrix} V_{fd} = U_{dreg}\frac{U_c}{2} \\ V_{fq} = U_{qreg}\frac{U_c}{2} \end{Bmatrix} \quad (3)$$

I_{Td} and I_{Tq} are the filtered output inverter current.

V_{fd} and V_{fq} are the modulated output inverter voltages.

V_{rd} and V_{rq} are the direct and quadrature measured grid voltages.

The grid voltages and currents in dq-axis are: V_{rd},V_{rq} , I_{Td} , and I_{Tq}.

The dq-frame constituents swapping function are: $\frac{U_{dreg}}{2}$ and $\frac{U_{qreg}}{2}$.

The relationship on the inverter DC side conferring to Kirchhoff's laws, are the Following:

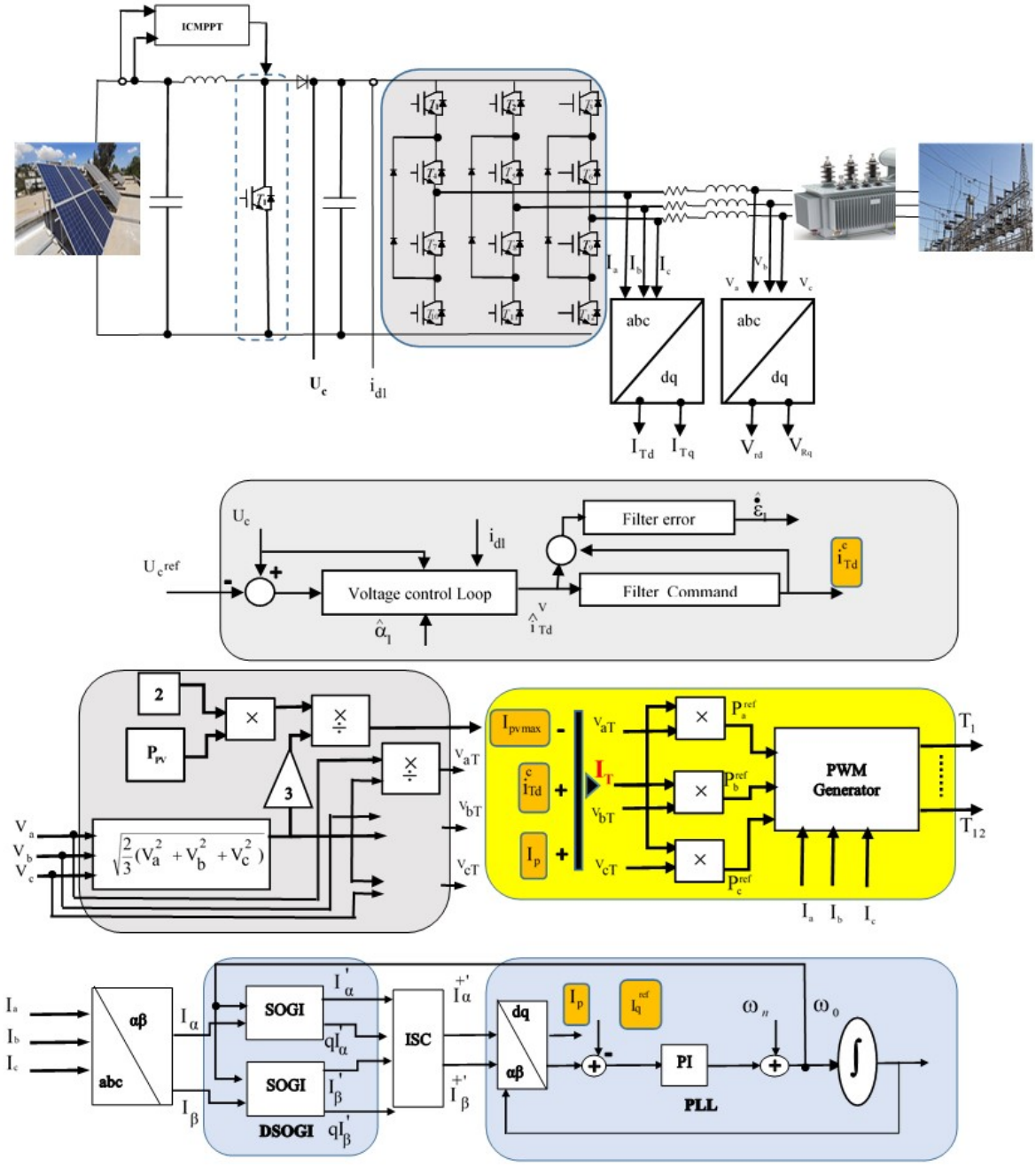

Fig. 1 Pv system and control modelling.

$$\begin{cases} c_i \frac{dU_{ci}}{dt} = I_{Ci}\ i = 1,2 \\ I_{c1} = I_{pv} - I_{d1} \Rightarrow\ c_1 \frac{dU_{c1}}{dt} = I_{pv} - I_{d1} \\ I_{c2} = I_{pv} + I_{d2} \Rightarrow c_2 \frac{dU_{c2}}{dt} = I_{pv} - I_{d2} \\ I_{c0} = I_{c1} - I_{c2} \Rightarrow I_{c0} = c_1 \frac{dU_{c1}}{dt} - c_2 \frac{dU_{c2}}{dt} \end{cases} \quad (4)$$

I_{pv} is the output current of the boost converter.

I_{d1} is the input current of the inverter.

Taking into account the energy preservation and ignoring the inverter power losses, the inverter in/out power equilibrium rapport among the DC and output side can be modelled as in Fig.2 and expressed as follows:

Where U_C is the DC-link voltage divided into two equal capacities,

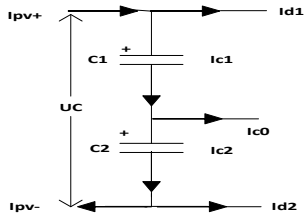

Fig. 2 DC Bus.

$$U_c . I_c = \frac{3}{2}(V_{rd} I_{Td} + V_{rq} I_{Tq}) \qquad , V_{rq} = 0 \quad (5)$$

$$C \frac{dU_c}{dt} = I_c - I_{d1} \quad (6)$$

$$\frac{dU_c}{dt} = \frac{I_c}{C} - \frac{I_{d1}}{C} \quad (7)$$

Knowing the fact, that V_{rq} average is equivalent to zero in steady state (from (5) we got $I_c = \frac{3}{2U_c}(V_{rd} I_{Td})$). Then, submitting (6) – (7), the DC-link voltage dynamics can be drowned as follow (8):

$$\frac{dU_c}{dt} = \frac{3 V_{rd} I_{Td}}{2 C U_c} - \frac{I_{d1}}{C} \quad (8)$$

Therefore, the PV grid-connected inverter's dynamic model system can be characterized as:

$$\begin{cases} \frac{dI_{Td}}{dt} = \frac{U_{dreg} U_c}{2 L_{Td}} - \frac{R_T}{L_{Td}} * I_{Td} + W_S * \frac{L_{Tq}}{L_{Td}} * I_{Tq} - \frac{V_{rd}}{L_{Td}} \\ \frac{dI_{Tq}}{dt} = \frac{U_{dreg} U_c}{2 L_{Tq}} - \frac{R_T}{L_{Tq}} * I_{Tq} - W_S * \frac{L_{Td}}{L_{Tq}} * I_{Td} - \frac{V_{rq}}{L_{Tq}} \end{cases} \quad (9)$$

We define in the mathematical model, R_T, L_{Tq} and C as values of resistance, inductance, and capacitance. Meanwhile measuring parameter's value truthfully, seems not easy throughout the present system the parameters could be kept as unidentified until they will be estimated in the estimation controller layer, which could be drawn as in (10):

$$\alpha_1 = \frac{1}{C}, \alpha_2 = \frac{R_T}{L_{Tq}}, \alpha_3 = \frac{1}{L_{Tq}} \quad (10)$$

Acquiescing (8), (9) and (10) we define the subsequent system

$$\begin{cases} \frac{dU_c}{dt} = \alpha_1 (\frac{3 V_{rd} I_{Td}}{2 U_c} - I_{d1}) \\ \frac{dI_{Td}}{dt} = \alpha_3 * V_{fd} - \alpha_2 * I_{Td} + W_S * I_{Tq} - \alpha_3 * V_{rd} \\ \frac{dI_{Tq}}{dt} = \alpha_3 * V_{fq} - \alpha_2 * I_{Tq} - W_S * I_{Td} - \alpha_3 * V_{rq} \end{cases} \quad (11)$$

From the expression (11) we carry out the controller estimated parameters α_1,α_2 , α_3. Then we will propose a backstepping adaptive command filtered with DSOGI method.

3. Controller design Backstepping

In order to maximize active power and consequently minimize reactive powers to the Point of Common Coupling PCC we generate controls V_{fd} and V_{fq} then generate I_{Td} and I_{Tq} reference values.

3.1 STEP 1 Errors definition

We the define errors $\varepsilon_i, i = 1..3$ hereunder;

$$\{\varepsilon_1 = u_C - u_C^{ref}\} \quad (12)$$

$$\{\varepsilon_2 = i_{Td} - i_{Td}^{ref}\} \quad (13)$$

$$\{\varepsilon_3 = i_{Tq} - i_{Tq}^{ref}\} \quad (14)$$

Where, u_C and u_C^{ref} are respectively the DC bus value and its reference.

i_{Td} and i_{Td}^{ref} are measured inverter dq frame direct current and the reference one.

i_{Tq} and i_{Td}^{ref} are measured inverter dq frame quadrature current and the reference one.

3.2 STEP 2 Lyapunov criterion application

The first Lyapunov function aiming to control and stabilize the DC bus will be written as follows:

$$K_1 = \frac{1}{2}\varepsilon_1^2 \quad (15)$$

we derive (12) and we inject (11) to it, the formula will be expressed such as:

$$\dot{\varepsilon}_1 = \alpha_1 \left(\frac{3 V_{rd} i_{Td}}{2 U_c} - i_{d1}\right) - \dot{U}_c^{ref} \quad (16)$$

The derivative expression of K_1 achieving the following:

$$\dot{K}_1 = \varepsilon_1 \dot{\varepsilon}_1 = \varepsilon_1 \left(\alpha_1 \left(\frac{3V_{rd} i_{Td}}{2U_C} - i_{d1} \right) - \dot{U}_c^{ref} \right) \quad (17)$$

The Lyapunov stability condition is imposed that $\dot{K}_1 \leq 0$. Additionally, the optimal choice of the virtual controller i_{Td}^V implies the best check.

$\dot{K}_1 = -\beta_1 \varepsilon_1^2$ with β_1 a positive constant. Formerly the virtual control is realized:

$$i_{Td}^V = \frac{2U_c}{3V_{rd}\alpha_1} \left(\alpha_1 i_{d1} + \dot{U}_c^{ref} - \beta_1 \varepsilon_1 \right) \quad (18)$$

The parameter α_1 remains unknown, subsequently, we estimate it and replace it by $\hat{\alpha}_1$ in (18):

$$\hat{i}_{Td}^V = \frac{2U_c}{3V_{rd}\hat{\alpha}_1} \left(\hat{\alpha}_1 i_{d1} + \dot{U}_c^{ref} - \beta_1 \varepsilon_1 \right) \quad (19)$$

We define the parameter estimation error as:

$$\tilde{\alpha}_1 = \alpha_1 - \hat{\alpha}_1$$

Based on (16) we have

$$(\hat{\alpha}_1 i_{d1} + \dot{U}_c^{ref}) = \hat{\alpha}_1 \frac{3V_{rd} i_{Td}}{2U_c} - \dot{\varepsilon}_1 \quad (20)$$

We inject (20) in (19) we obtain

$$\dot{\varepsilon}_1 = \frac{3V_{rd}\hat{\alpha}_1 (i_{Td} - \hat{i}_{Td}^V)}{2U_c} - \beta_1 \varepsilon_1 \quad (21)$$

The proposed command Filter is described below:

Its Transfer Function TF expressed by (22) and (23)

$$H = \frac{X_c}{X_d} = \frac{k\omega_n^2}{S^2 + 2\xi\omega_n + \omega_n^2} = \frac{1}{\frac{S^2}{\omega_n^2} + \frac{2\xi S}{\omega_n} + 1} \quad (22)$$

$$\begin{bmatrix} \dot{X}_1(t) \\ \dot{X}_2(t) \end{bmatrix} = \begin{pmatrix} 0 & 1 \\ 0 & -2\xi\omega_n \end{pmatrix} \begin{bmatrix} X_1(t) \\ X_2(t) \end{bmatrix} + \begin{pmatrix} 0 \\ \omega_n^2 \end{pmatrix} U$$
$$Y(t) = (1 \quad 0) \begin{bmatrix} X_1(t) \\ X_2(t) \end{bmatrix} \quad (23)$$

We define $\begin{bmatrix} X_1 \\ X_2 \end{bmatrix} = \begin{bmatrix} x^c \\ \dot{x}^c \end{bmatrix}, U = x^d$ (24)

The TF is very sensitive if we act on its poles and zeros by any modification of derivative or integral knowing that the FT reaction will be very arbitrary. Then for this purpose a preliminary study is required from time derivative, structure control diagram and the state equation.

$$\dot{\hat{\varepsilon}}_1 = -\beta_1 \hat{\varepsilon}_1 + \frac{3V_{rd}\hat{\alpha}_1 (i_{Td}^{ref} - \hat{i}_{Td}^V)}{2U_c} \quad (25)$$

Using (16) and (25) It could be figured out as:

$$\dot{\tilde{\varepsilon}}_1 = \dot{\varepsilon}_1 - \dot{\hat{\varepsilon}}_1 = \frac{3V_{rd}\hat{\alpha}_1 (i_{Td} - \hat{i}_{Td}^V)}{2U_c} - \beta_1 \varepsilon_1 - \frac{3V_{rd}\hat{\alpha}_1}{2U_c} \left(i_{Td}^{ref} - \hat{i}_{Td}^V \right) + \beta_1 \hat{\varepsilon}_1 \quad (26)$$

Knowing that $\begin{cases} \alpha_1 = \tilde{\alpha}_1 + \hat{\alpha}_1 \\ \dot{\varepsilon}_1 = \dot{\tilde{\varepsilon}}_1 + \dot{\hat{\varepsilon}}_1 \end{cases}$, (26) becomes:

$$\dot{\tilde{\varepsilon}}_1 = \frac{3V_{rd}\hat{\alpha}_1 \varepsilon_2}{2U_c} + \tilde{\alpha}_1 \left(\frac{3V_{rd} i_{Td}}{2U_c} - i_{d1} \right) - \beta_1 \tilde{\varepsilon}_1 \quad (27)$$

4. DSOGI Filter approach

The control approach implementation is described in Fig.3 Both of chopper and inverter own their distinct control. The PV generator voltage Vpv and current Ipv are firstly sensed, then applied to the INC MPPT controller entree. The last cited controller sets up the PV array set point voltage which is equivalent to the DC link voltage. Meanwhile, it assures the impedance adaptation by defining the boost converter duty ratio. At the end of line, we obtain the switching pulses by comparing the duty ratio and the 5Khz frequency sawtooth waveform.

The control technique needs the grid currents sensing I_α and I_β ; The PCC voltages V_a, V_b and V_c; load currents if there are local loads and the DC link voltage U_c. The VSC input voltage is accustomed adoptively according to the PCC voltage for minimum VSC switching losses. The sensed grid currents are compared with generated reference currents in a current controller, and the switching pulses for VSC are obtained. The VSC control needs generation of four quantity namely, active power current component, PV dynamic current, DC link voltage loss current component, and unit templates for the synchronization of PV converter to the distribution grid.

Unit templates Generation: Since we have the three grid phase voltages V_a, V_b and V_c :

The PCC voltage amplitude is estimated at:

$$V_T = \sqrt{\frac{2}{3}(V_a^2 + V_b^2 + V_c^2} \quad (28)$$

The unit templates for the three-utility grid voltage are evaluated as:

$$\begin{Bmatrix} V_{aT} = \frac{V_a}{V_T} \\ V_{bT} = \frac{V_b}{V_T} \\ V_{cT} = \frac{V_c}{V_T} \end{Bmatrix} \quad (29)$$

Dynamic PV current $I_{pv\max}$: The PV panel voltage V_{pv} and PV panel current I_{pv} are sensed, and the PV array power is written as:

$$P_{pv} = V_{pv} \times I_{pv} \quad (30)$$

$$I_{pv\max} = \frac{2P_{pv\max}}{3V_T} \quad (31)$$

The PV dynamic current is given as in Fig. 2

Active current estimation component: In the three-phase system, the stationary α axis and β axis load current component $I_{\alpha\beta} = \begin{bmatrix} I_\alpha \\ I_\beta \end{bmatrix}$ are formulated in terms of various phases as:

$$\begin{bmatrix} I_\alpha \\ I_\beta \end{bmatrix} = \frac{1}{\sqrt{3}} \begin{bmatrix} \frac{2}{\sqrt{3}} & -\frac{1}{\sqrt{3}} & -\frac{1}{\sqrt{3}} \\ 0 & \frac{1}{\sqrt{3}} & -\frac{1}{\sqrt{3}} \end{bmatrix} \begin{bmatrix} I_a \\ I_b \\ I_c \end{bmatrix} \quad (32)$$

The axes α and β axis currents voltages $I_\alpha(k)$ and $I_\beta(k)$ remain distorted. The in-phase and quadrature harmonic free positive sequence HFPS and harmonic free negative sequence HFNS currents are mined from the last cited distorted currents $I_\alpha(k)$ and $I_\beta(k)$ by adding DSOGI filter. Its signal stream chart is shown in Fig. 5.

4.1 The first order prefilter TF

$$H_{CL}(p) = \frac{\omega_f}{p+\omega_f} \quad (33)$$

Is the closed loop standard, low pass transfer function which has a unity gain, where w_f is the cutoff angular frequency. We know that this first order scalar filter isn't an optimal pre-grid filter. Then, it's intuitive to put the right frequency by modifying $p = p - jw_0$ with w_0 is the angular grid frequency equal to ^{100p} as written in Fig. 3 and Fig. 4.

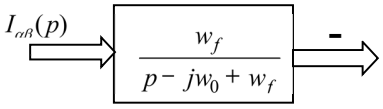

Fig. 3 Modified first order prefilter in closed loop.

$$H_{CL}(p) = \frac{\omega_f}{p - jw_0 + \omega_f} \quad (34)$$

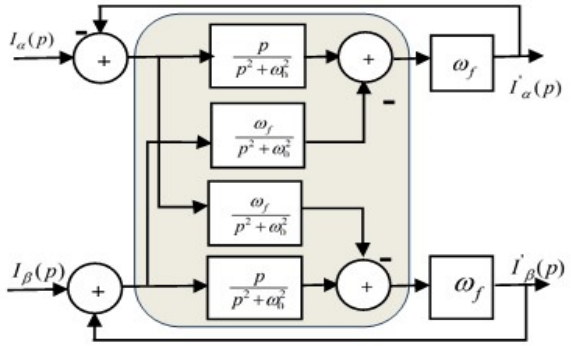

Fig.4 Equivalent modified first order prefilter in closed loop.

The DSOGI scalar open loop transfer function as shown in Fig. 5and Fig. 6 of the $H_{OL}(p)$ is expressed as:

$$H_{OL}(p) = \frac{\omega_f}{p - j\omega_0} = \frac{\omega_f p}{p^2+\omega_0^2} + j\frac{\omega_f \omega_0}{p^2+\omega_0^2} = R(p) + j\mathrm{Im}(p) \quad (35)$$

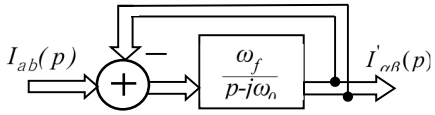

Fig. 5 Modified first order prefilter in open loop.

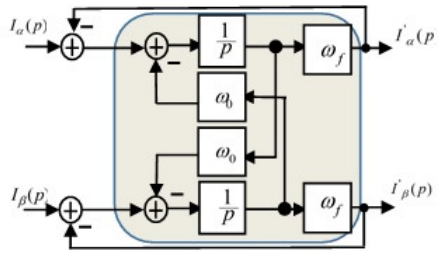

Fig. 6 Equivalent modified first order prefilter in open loop.

$$I'_{\alpha\beta}(p) = H_{OL}(p) \times I_{\alpha\beta}(p) = (R(p) + j\mathrm{Im}(p)) \times (I_\alpha(p) + j \times I_\beta(p)) \quad (36)$$

Therefore,

$$\begin{Bmatrix} I'_\alpha(p) = R(p).I_\alpha(p) - \mathrm{Im}(p).I_\beta(p) \\ I'_\beta(p) = R(p).I_\beta(p) + \mathrm{Im}(p).I_\alpha(p) \end{Bmatrix} \quad (37)$$

$$\begin{Bmatrix} I'_\alpha(p) = I_\alpha(p).\frac{p}{p^2+\omega_0^2} - I_\beta(p).\frac{\omega_0}{p^2+\omega_0^2} \\ I'_\beta(p) = I_\alpha(p).\frac{\omega_0}{p^2+\omega_0^2} + I_\beta(p).\frac{p}{p^2+\omega_0^2} \end{Bmatrix} \quad (38)$$

$$I'_{\alpha}(p) + j.I'_{\beta}(p) = \left(\frac{I_{\alpha}(p)+j.I_{\beta}(p)}{p-j\omega_0}\right) \quad (39)$$

$$I'_{\alpha\beta}(p) = H_{OL}(p) \times I_{\alpha\beta}(p) = (R(p) + j\mathrm{Im}(p)) \times (I_{\alpha}(p) + j \times I_{\beta}(p)) \quad (40)$$

4.2 The second order DSOGI prefilter

The first-order DSOGI prefilter can only reduce but not remove definitely the HFNS. Consequently, under sternly unbalanced grid conditions its performance might not be suitable. Moreover, if we add a complex zero pz = −jω0 into (33); we will directly produce a fundamental negative frequency zero gain which marks the HFNS elimination. Nonetheless, the harmonic attenuation of the last cited complex filter will be visibly reduced due to the TF numerator increased order. Therefore, taking into account both of HFNS and harmonic attenuation elimination a second order DSOGI prefilter with a complex zero

pz = −jω0 will be drawn as:

$$H(p) = \frac{G(\mathrm{p} + j\omega_0)}{p^2+2m\omega_n\mathrm{p} + \omega_n{}^2} \quad (41)$$

Where m is the damping ratio, ωn presents the undamped natural angular frequency, and G is an adjustable gain. For the HFNS extraction purpose, it is required that :

$$|H(p)| = |H(jw)| = 1H(p) = \frac{G(j\omega_0+j\omega_0)}{(j\omega_0)^2+2m\omega_n j\omega_0+\omega_n{}^2} = 1 \quad (42)$$

$$2j\omega_0 G = \omega_n{}^2 - \omega_0{}^2 + 2m\omega_n j\omega_0 \quad \left\{\begin{matrix}\omega_n = \omega_0 \\ G = m\omega_n = m\omega_0\end{matrix}\right\} \quad (43)$$

Investigating the imaginary and real parts from both sides of (41) gives:

$$H(p) = \frac{m\omega_{.0}(\mathrm{p} + j\omega_0)}{p^2+2m\omega_0\mathrm{p} + \omega_0{}^2} \quad (44)$$

In practice, we usually set m to 0.707 in order to get an optimal dynamic performance.

In the implementation of this SOF, we have adopted the DSOGI-Based Prefilter design [16].

4.3 DSOGI-Based Prefilter

The block diagram of the DSOGI-based prefilter is shown in Fig. 7, where $I'^{+}_{\alpha}, I'^{+}_{\beta}, I'^{-}_{\alpha}, I'^{-}_{\beta}$, are the calculated FPC and FNC, Respectively; SOF-α and SOF-β represent the α- and β-axis second-order scalar filters (SOFs), respectively.

Since SOF-α and SOF-β are in the same structure, the SOF-α scalar transfer functions are given as:

$$\left\{\begin{matrix} I'_{\alpha}(p) = \frac{2\omega_0 p}{p^2+2m\omega_0\mathrm{p}+\omega_0{}^2} I_{\alpha}(p) \\ qI'_{\alpha}(p) = \frac{2jm\omega_{.0}2}{p^2+2m\omega_0\mathrm{p}+\omega_0{}^2} I_{\alpha}(p) \end{matrix}\right\} \quad (45)$$

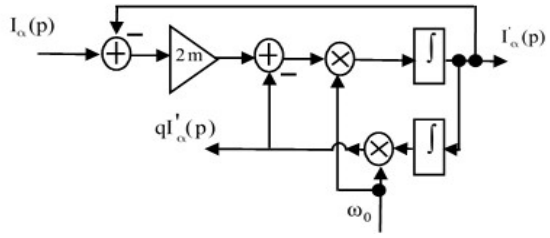

Fig. 7 Second order filter scalar SOFs.

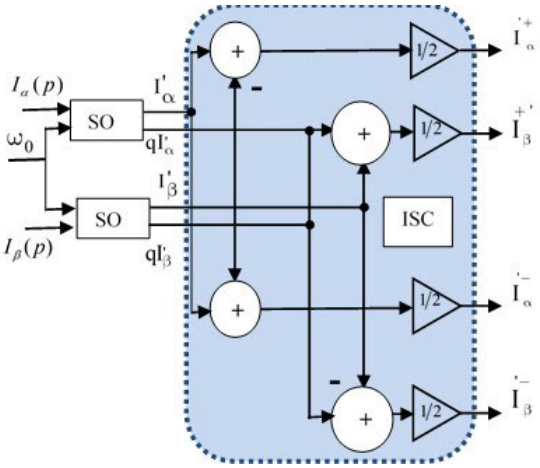

Fig. 8 DSOGI based prefilter with ISC calculator.

Moreover, the instantaneous symmetrical component ISC calculation unit as revealed in Fig. 8. According to the ISC method, the unbalanced three-phase grid voltages can be resolved into their symmetrical components through Fortescue method.

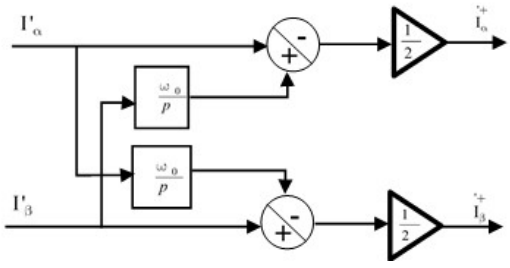

Fig. 9 DSOGI based prefilter with ISC calculator.

The ISC calculation in α − β reference frame, as shown in Fig. 9, is given as:

$$I'^{+}_{\alpha\beta} = \begin{bmatrix} 1 & -q \\ q & 1 \end{bmatrix} I'_{\alpha\beta}$$
$$I'^{-}_{\alpha\beta} = \begin{bmatrix} 1 & q \\ -q & 1 \end{bmatrix} I'_{\alpha\beta} \quad (46)$$

Where q is a $\frac{\pi}{2}$ lagging phase-shift operator and $I'^{+}_{\alpha\beta}$ and $I'^{-}_{\alpha\beta}$ are respectively the complex fundamental positive and negative-sequence. It can be seen that q is equal to $\frac{w_0}{p}$ in the SOF-α. Furthermore, the HFNS calculation in the DSGOI-prefilter can be redrawn as:

$$I'^{+}_{\alpha\beta} = \frac{1}{2}(1 + j\frac{w_0}{p}) I'_{\alpha\beta} \quad (47)$$

$$I'^{+}_{\alpha\beta} = \frac{1}{2}\left(1 + j\frac{w_0}{p}\right) \frac{2m\omega_{.0}p}{p^2 + 2m\omega_0 \mathrm{p} + {\omega_0}^2} I_{\alpha\beta}$$
$$= \frac{m\omega_{.0}(\mathrm{p} + j\omega_0)}{p^2 + 2m\omega_0 \mathrm{p} + {\omega_0}^2} I_{\alpha\beta} \quad (48)$$

$$I'^{-}_{\alpha\beta} = \frac{1}{2}(1 - j\frac{w_0}{p}) \frac{2m\omega_{.0}p}{p^2 + 2m\omega_0 \mathrm{p} + {\omega_0}^2} I_{\alpha\beta}$$
$$= \frac{m\omega_{.0}(\mathrm{p} - j\omega_0)}{p^2 + 2m\omega_0 \mathrm{p} + {\omega_0}^2} I_{\alpha\beta}$$

Consequently, the DSOGI-based prefilter complex transfer functions could be found at:

$$I'^{+}_{\alpha\beta} = \frac{m\omega_{.0}(\mathrm{p} + j\omega_0)}{p^2 + 2m\omega_0 \mathrm{p} + {\omega_0}^2} I_{\alpha\beta}$$
$$I'^{-}_{\alpha\beta} = \frac{m\omega_{.0}(\mathrm{p} - j\omega_0)}{p^2 + 2m\omega_0 \mathrm{p} + {\omega_0}^2} I_{\alpha\beta} \quad (49)$$

$I'^{+}_{\alpha\beta}(\mathrm{p})$ and $I'^{-}_{\alpha\beta}(\mathrm{p})$ are respectively the governing HFPS and HFNS complex transfer functions. Moreover, we notice from (48) that

$I'^{+}_{\alpha\beta}(\mathrm{p})$ and $I'^{-}_{\alpha\beta}(\mathrm{p})$ made from the same SOF except a minus difference in the complex zeros. We have at the end DSOGI-based prefilter is, in fact, itself the SOF.

The HFPS current components $I'^{+}_{\alpha}(\mathrm{p})$ and $I'^{+}_{\beta}(\mathrm{p})$ (s) are utilized to derive the active power current component and reactive current power component as,

$$\begin{bmatrix} I_p \\ I_q \end{bmatrix} = \begin{bmatrix} \cos\omega_0 t & \sin\omega_0 t \\ \sin\omega_0 t & \cos\omega_0 t \end{bmatrix} \begin{bmatrix} I'^{+}_{\alpha} \\ I'^{+}_{\beta} \end{bmatrix} \quad (50)$$

Reference Angle Grid and Frequency Estimation: The estimated HFPS components are not orthogonal in case of large drift in grid frequency, and thus, the extracted active power component of load current/voltages is inaccurate. Thus, the utility grid frequency accurate estimation is essential under frequency drift condition with minimum overshoot and minimum settling time. The accurate estimation governing equations with an optimal dynamic response is as:

$$\omega_0 = \omega_n + \int k_i (I_q - I^{ref}\mathrm{q}) \quad (51)$$
$$\theta = \int (\omega_0 + k_p (I_q - I^{ref}\mathrm{q}) \quad (52)$$

Grid References current Estimation: The real grid current is given as:

$$I_T = \mathrm{i}^{c}_{Td} + I_p - I_{pv\max} \quad (53)$$

The three phase grid reference currents are estimated using the active power grid current as,

$$\begin{Bmatrix} P_a^{ref} = I_t \times V_{aT} \\ P_b^{ref} = I_t \times V_{bT} \\ P_c^{ref} = I_t \times V_{cT} \end{Bmatrix} \quad (54)$$

Comparing these grid reference currents with the sensed ones through the comparator then fed to the current controller could lead to the reference VSC control switching sequences.

5. Simulation results and discussion

We developed a PV generator constituted by 5 series modules and 66 parallel strings providing 100.8 kW generated power (64*5*5=1600) module. This PV field is done in our previous works [17, 18].

We considered the following sunlight profile which we presume that its dynamic is higher than a cloud crossing clear sky to be sure about our control performance. Indeed, the irradiation profile begins from 1000 w/m² during 2 seconds, decreases from 1000 w/m² to 200 w/m² for 2 seconds and regains 1000 w/m².

PVG: After unlocking control at 0.02s the power reaches the MPP, as drawn in Fig. 10, which means that it tracks the irradiation profile.

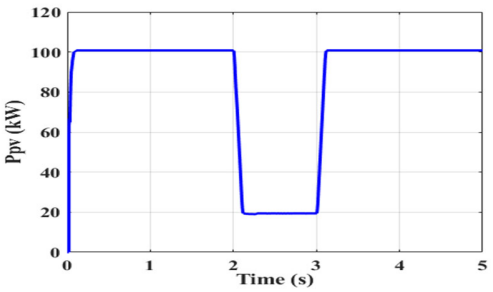

Fig. 10 Generated PV power.

Fig. 11 shows the evolution of the mean errors in output of boost controllers, reveling a fast-responding time.

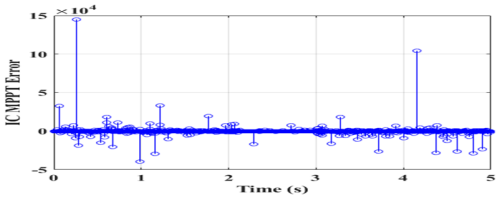

Fig. 11 Mean ICMPPT error.

The mean error evolution in boost controller output of Fig. 11 proves a fast-responding time and minimal error.

Bus:

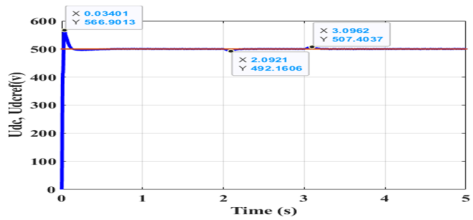

Fig. 12 Continuous bus Voltage.

Fig. 12 demonstrate the DC bus voltage dynamics set point has within 0.1s thanks to the filtered DSOGI and backstepping action. In the range of 0.1 s to 2 s when the sunlight, even drops at t=2s or raised up at=3s, the voltage stays unaffected at its reference value is 500V. Even for extremely sudden climate changes the bus voltage maintains its reference.

In comparison with [16, 19-25] we mitigate the first overshoot to 566 V against 1300V when the reference bus value was 750 V and 622V in our previous works with the PID use [18], which could be fatal for the bus. A comparison is performed below in Table 1.

Table.1 DC-bus different control techniques comparison

First DC bus overshoot	***Voltage (V)***
Filtered Backstepping-DSOGI	566V
DSOGI [17]	1300 V
PID [18-19]	622

5.1 Reference grid component synthesis

Fig. 13 and Fig. 14 are park transform of our POC voltages and currents which we aim to reproduce for control purpose.

The synthesized Itd, Itq, Vrd and Vrq magnitudes have been set by the performed command law respectively to 0.4pu, 0pu, 1.2pu and 0pu for the quadratic component. Therefore, we effort just the active power flow through the POC.

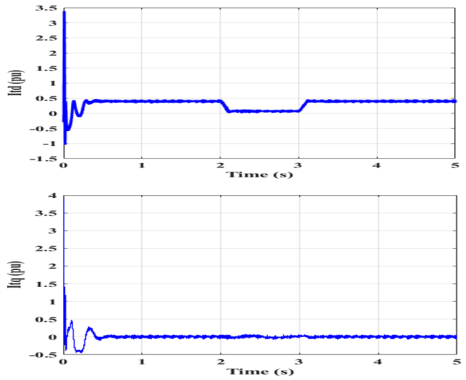

Fig. 13 Reference currents in dq frame.

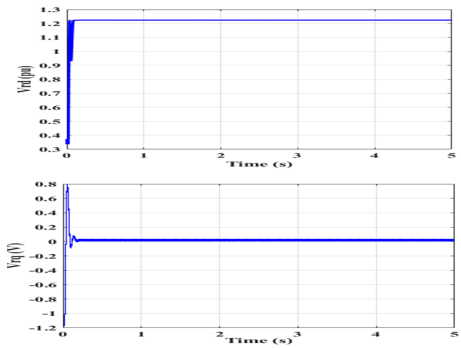

Fig. 14 Reference voltages in dq frame.

5.2 Backstepping

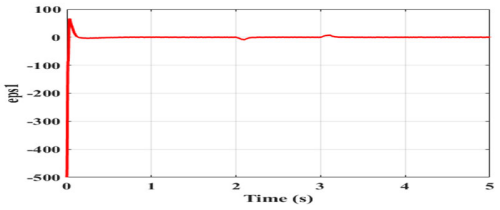

Fig. 15 Bus error ε_1.

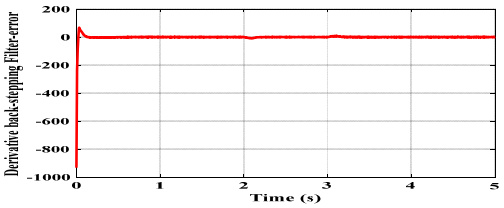

Fig. 16 Backstepping derivative filter error $\hat{\dot{\varepsilon}}_1$.

The error between the bus voltage and its reference ε_1 presented by Fig. 15 as well the filtering error $\hat{\dot{\varepsilon}}_1$ in Fig.

16 are converging straight to 0 which indicates that the backstepping applied method is robust and trustworthy.

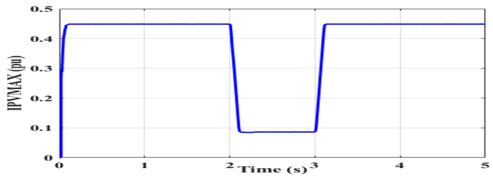

Fig. 17 Current IPVMAX.

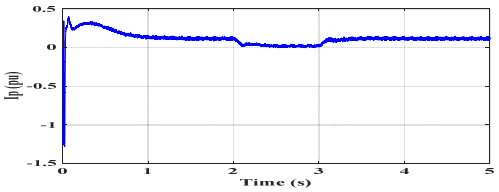

Fig. 18 Current IP .

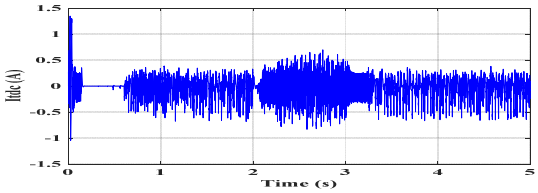

Fig. 19 Current ITdc.

We gather the 3 currents IPVMAX (Fig. 17), IP (Fig. 18) and ITdc (Fig. 19) producing the total current IT in order to generate the reference powers that will attack the entree of the PWM generator.

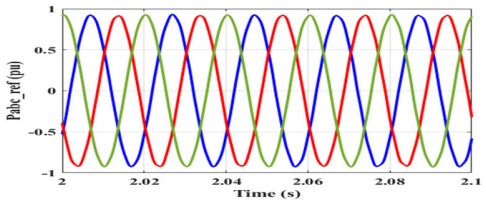

Fig. 20 Reference powers in pu.

Fig. 20 shows Paref, Pbref, Pcref, which are reference voltages aiming to generate output pulses that will be applied to IJBT gates.

5.3 DSOGI_ISC

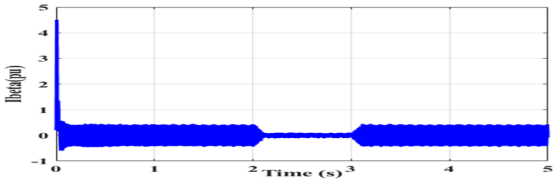

Fig. 21 Concordia currents transform in pu.

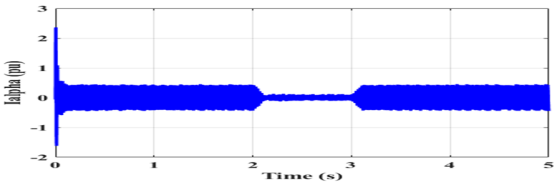

Iα and Iβ are Concordia transform of the three grid currents that will be presented to DSOGI entrees.

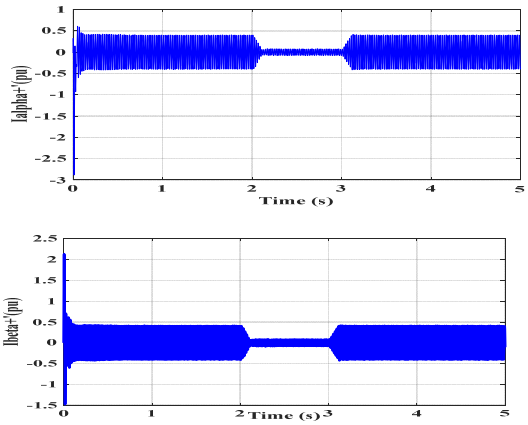

Fig. 22 DSOGI positive sequence output currents in pu.

At Fig. 22 the DSOGI output we obtain the HFNS and HFPS, we exploited just the HFPS to originate the active power current and reactive current power components.

5.4 PLL

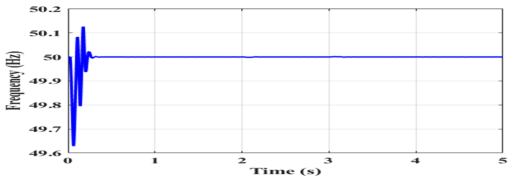

Fig. 23 DSOGI positive sequence output currents in pu.

From Fig. 23 we notice the frequency controls are responding fast in less than 0.2s from the beginning of control action and it remains 50 Hz throughout the simulation same as the grid angle in Fig.24 guaranteeing that the chain is synchronized with the grid frequency and angle.

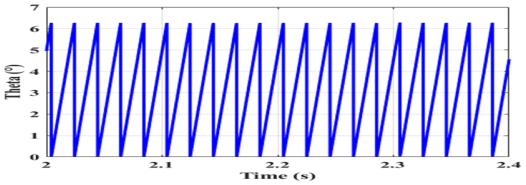

Fig. 24 DSOGI positive sequence output currents in pu.

5.5 GRID

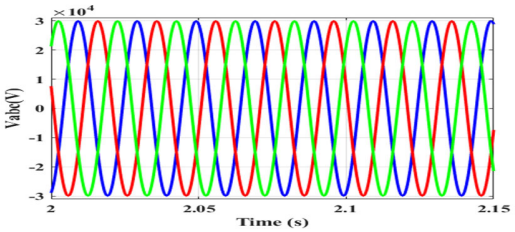

Fig. 25 DSOGI positive sequence output currents in pu.

Fig. 25 exposes the voltage waveform at the POC independently of sunlight nature intermittent. Additionally, it's inside the acceptable Voltage directives range 30KV+-5%, even in t=2.1s and/or t=3.1s which are illumination transitions (1000, 200 and 1000w/m²).

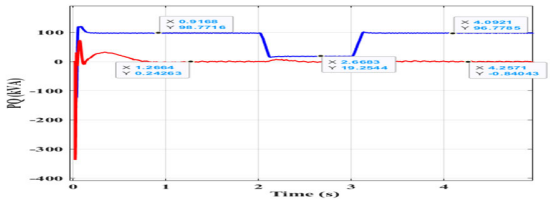

Fig. 26 DSOGI positive sequence output currents in pu.

Fig. 26 presents the received power at POC is 97 KW from 100 KW generated. This explicates a yield of approximately 97%. And an acceptable power factor almost close to unity.

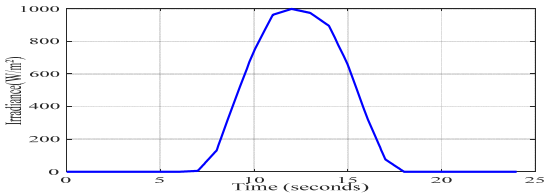

Fig. 27 Irradiance profile.

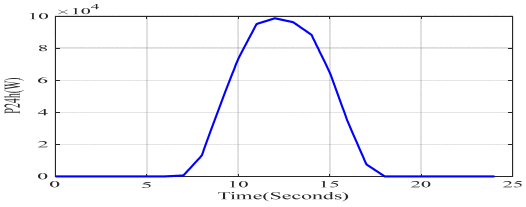

Fig. 28 Power at the PCC over 24 hours.

Fig.27 and Fig.28 present respectively the irradiance profile and the generated power over 24. The received power at POC is 97 KW from 100 KW generated at midday. This last figure demonstrates the power evolution throughout the day and implicitly command uphold.

6. Conclusion

This paper underlines a total power injected PVG to an HTA grid-connected three-phase system. First of all, we presented the different mathematical used models and technics along with a detailed DSOGI and backstepping study and finally we record the overall system simulation response. The last cited suitable control laws mix reaches the anticipated production. This energy transfer optimization leads to get an appropriate waveform quality produced by the multi-level three phase NPC inverter. Adding to that, we ensured an optimal bus first overshoot preserving its right work, life duration and security. An amelioration has been getting compared to related works in bus voltage value and then power transfer quality. As a future work we are focusing on implementing the presented control laws using a Raspberry PI 4 card in a manner that could be tested in a real environment.

References

[1] Zini, G., Mangeant, C., and Merten, J.: Reliability of large-scale grid-connected photovoltaic systems, Renewable Energy, vol. 36 (9), pp. 2334-2340 (September 2011)

[2] Reddy, V. R. and Sreeraj, E. S.: A Feedback-Based Passive Islanding Detection Technique for One-Cycle-Controlled Single-Phase Inverter Used in Photovoltaic Systems, IEEE Trans. on Industrial Electronics, vol. 67(8), pp. 6541-6549 (September 2019).

[3] Karimi, M., Farshad, M., Hong, Q., and Laaksonen, H., Kauhaniemi, K.: An Islanding Detection Technique for Inverter-Based Distributed Generation in Microgrids, Energies, vol. 14(1), pp. 1-18 (2021)

[4] Dezhi, Xu., Gang, W., Wenxu, Y., and Xinggang, Y.: A novel adaptive command-filtered backstepping sliding mode control for PV grid-connected system with energy storage, Solar Energy, vol. 178, pp. 222-230 (January 2019)

[5] Jiang, J., Li, H., Zhao, K., Cao, D. and Guirao, J. L. G.: Finite time stability and sliding mode control for uncertain variable fractional order nonlinear systems, Adv Differ Equ, vol. 127(2021), pp. 1-16 (2021).

[6] Hussain, S. K., Muhammad, A., Kimmo, K., and Mohsin, M.: Improved finite control set model predictive control for distributed energy resource in islanded microgrid with fault-tolerance capability, Engineering Science and Technology, an International Journal, vol. 24(3), pp. 694-705 (June 2021)

[7] Mahdi, S. and Vahid, J. M.: A Robust Finite-time Fault-tolerant Formation Control of Stochastic Multi-agent Systems in the Mean-Square Sense, 2020 28th Iranian Conference on Electrical Engineering (ICEE), pages 1-5, 4-6 Aug(2020)

[8] Guo, J., Nai, Y. and Yang, Q.: Adaptive Command Filtered Backstepping Control for Uncertain Nonlinear Systems and

Its Application to Wind Turbine, 2020 39th Chinese Control Conference (CCC), pp. 340-345 (2020)
[9] Mohamed, O. G., Ahmed, H. H. and Ayman, A. El.: Command-Filtered Backstepping Control of Multitank System, 2019 7th International Conference on Control, Mechatronics and Automation (ICCMA), pp.73-77 (Nov. 2019)
[10] Guixian, Xu., Jian, Li., and Jialu, Du.: Robust adaptive command-filtered backstepping synchronization navigation control with prescribed performance for supply ship during underway replenishment, 2021, J Mar Sci Technol (2021)
[11] Xin, Z., Chuang, G., Zhi-gang, L., Xin-yu, O., and Li-bing, W.: Observer-based adaptive fuzzy finite-time prescribed performance tracking control for strict-feedback systems with input dead-zone and saturation, Nonlinear Dynamics, vol. 103 (2), pp. 1645-1661 (2021)
[12] Leon, J. I., Vazquez, S. and Franquelo, L. G.: Multilevel Converters: Control and Modulation Techniques for Their Operation and Industrial Applications, Proceedings of the IEEE, vol. 105(11), pp. 2066 (Nov. 2017)
[13] Yan, C., Chen, J., Liu, H. and Lu, H.: Model-Based Fault Tolerant Control for the Thermal Management of PEMFC Systems, IEEE Transactions on Industrial Electronics, vol. 67(4), pp. 2875-2884 (2020)
[14] Swaroop, D., Hedrick, J. K., Yip, P. P. and Gerdes, J. C.:Dynamic surface control for a class of nonlinear systems, IEEE Transactions on Automatic Control, vol. 45(10), pp. 1893-1899(Oct. 2000)
[15] Jinpeng, Y., Peng, S., and Lin, Z.: Finite-time command filtered backstepping control for a class of nonlinear systems, Automatica, vol. 92(2018), pp. 173-180 (2018)
[16] Weiwei, L., Xinbo, R., Chenlei, B., Donghua, P., and Xuehua, W.: Grid Synchronization Systems of Three-Phase Grid-Connected Power Converters: A Complex-Vector-Filter Perspective,IEEE Trans. on Industrial Electronics, vol. 61(4), pp 1855-1870(2014)
[17] Rofiatul, I., Subiyanto, S., and Dhidik, P.: Improvement of DSOGI PLL Synchronization Algorithm with Filter on Three-Phase Grid-Connected Photovoltaic System, Jurnal Elektronika dan Telekomunikasi (JET), 2018, vol. 18, pp. 35-4(2018).
[18] Benabdallah, I. and Cherif, A.: Improved Modeling and Control of a HTA Grid Connected 500 KW PV Systems, Indian Journal of Science and Technology, vol. 10(27), pp.1-10(July 2017).
[19] Benabdallah, I., Oun A., and Cherif, A.: Grid Connected PV Plant based on Smart Grid Control and Monitoring, (IJACSA) International Journal of Advanced Computer Science and Applications, vol. 8(6),(2017)
[20] Bleijs, J.A.M. and Gow, J.A.: Fast maximum power point control of current-fed DC-DC converter for photovoltaic arrays, Electronics Letters, vol. 37(1), p. 5 –6(2001)
[21] Jeong, J.B. and Kim, H.J. : Active anti-islanding method for PV system using reactive power control, Electronics Letters, vol. 42(17), pp. 1004 – 1005(2006).
[22] Bor-Ren, L.: Resonant Converter with Wide Input Voltage Range and Input Current Ripple-Free, Electronics Letters, vol. 54 (18)
[23] Xiaohe, W. and Dan, S.: Multi-objective self-synchronised virtual synchronous generator in unbalanced power grid Multi-objective self-synchronised virtual synchronous generator in unbalanced power grid, Electronics Letters, vol. 54(18) , (2018)
[24] Kaisar, R. K., Yazed A. S., Atiqur R., Muhammad, S. S., and Ali, O.E.: Condition Monitoring and Control of a Campus Microgrid Elements, IJCSNS, vol.19 (2), pp. 155-162 (February 2019)
[25] Oun, A., Benabdallah, I., and Adnene, C. Analysis and design of a grid connected real plant in Libya using ETAP software. IJCSNS, vol.18(3), pp. 31-40 (2018)

Salim Nebili Was born in Gafsa,Tunisia, in 1973. He received the engineering degree from the national engineering scool of Gabes (ENIG) in 1998 and Master degree in 2002 from the national engineering school of Tunis (ENIT). Member of Analysis and treatment of electrical and energetic signals and systems laboratory, managed by Pr.Dr. Adnen Cherif. His research interests include Electrical engineering, Renewable energies and Smart-Grids.

Ibrahim Benabdallah Was born in Tunis, Tunisia, in 1984. He received the Master and Doctor's degree in Electronics from the Faculty of Sciences of Tunis (FST). Member of Analysis and treatment of electrical and energetic signals and systems laboratory, managed by Pr.Dr. Adnen Cherif. His research interests include Electrical engineering, Renewable energies and Smart-Grids.

Adnane Cherif Received the engineer, master and doctorate degrees from the National Engineering School of Tunis (ENIT), in Tunisia, he is a senior Professor Doctor at the Science Faculty of Tunis and responsible of Analysis and treatment of electrical and energetic signals and systems ATEESS Laboratory in Faculty of Science of Tunis, Tunisia. His fields of interest, concern digital signal processing and speech processing, energetic systems, renewable energies and Smart-Grids